ADVANCED OPTICAL MATERIALS
www.advopticalmat.de

Phonon Polaritons: A New Paradigm for Light-Controllable Heat Sources

*Bei Yang, Deng Pan, and Qing Dai**

Photothermal applications, such as therapy, imaging, and catalysis, necessitate heat sources capable of generating high temperatures under mid-infrared (mid-IR) illumination. However, commonly used metal nanostructures suffer from low efficiency due to their high carrier concentrations, resulting in shallow surface heating and optical range restrictions. To overcome these limitations, this work proposes a novel approach employing materials that support phonon polaritons (PhPs) as a promising paradigm for light-controllable heat sources. The theoretical demonstration reveals that hexagonal boron nitride (hBN) nanorods can produce up to 46 times more heat compared to plasmonic gold counterparts under resonant monochromatic light. This superior heating capability stems from the unique properties of PhPs, which enable stronger field confinement and deeper penetration within the nanostructure, leading to higher efficiency by circumventing the electrostatic shielding effect associated with plasmonic heating. Furthermore, this work demonstrates that the heating performance of hBN antennas can be optimized by manipulating their size, geometry, and material loss. Notably, the use of isotopically pure hBN can triple the heat power. These findings highlight the tremendous potential of hBN antennas as light-controllable heat sources, opening up new possibilities for IR photothermal applications by harnessing materials that support PhPs.

1. Introduction

Light-controllable heat sources at the nanoscale, particularly those powered by infrared (IR) light, hold immense promise in various fields including photothermal therapy, imaging, and catalysis.[1–5] Mid-IR light offers the advantages of deeper tissue penetration and the ability to resonantly excite molecular vibrations compared to visible light.[1,6–8] However, conventional metal nanostructures, which generate heat through the damping of localized surface plasmons (LSPs) in a phenomenon known as thermoplasmonics,[9–13] exhibit low photothermal conversion efficiency in the mid-IR range. This inefficiency arises from their high carrier concentrations and thin skin depth (approximately 20 nm for gold), which restrict their light absorption and electric field enhancement to the optical range and superficial surface layers.[14–16] To achieve optimal plasmonic heating, metal nanostructures need to be small or thin (typically 10–100 nm) and densely packed.[17,18] Yet, these requirements pose challenges including easy aggregation, costly fabrication, and poor stability, as observed in plasmonic colloidal solutions or patterned metamaterials.[11,19–21] Consequently, there is a growing demand for alternative materials that can overcome these limitations and provide effective light-controllable heat sources operating under mid-IR illumination.

Polar dielectrics have demonstrated superior light trapping capabilities in the IR range compared to metals by leveraging phonon polaritons (PhPs).[22,23] PhPs are quasiparticles formed through the strong coupling of incident photons with optical phonons in these materials. Unlike LSPs in metal nanostructures, PhPs in polar dielectrics exhibit significantly lower material loss due to the longer lifetime of phonons relative to free electrons.[24] This is reflected by the small imaginary part of the permittivity ($\mathrm{Im}(\epsilon)$) of polar dielectrics and has been evidenced by the large quality factors of sub-diffraction photonic nanostructures.[25,26] Consequently, PhPs have emerged as low-loss alternatives to LSPs, particularly in the realm of IR nanophotonics.[27] In this context, previous studies have often assumed that the heat generation from PhP decay is negligible.[27] However, we note that low material losses do not necessarily imply low photoinduced heating.[28] To be more precise, the photoinduced heat power depends on both the material losses and the detailed field distribution inside the nanostructure, i.e. $Q_h \propto Im(\varepsilon)\iiint |E|^2 dV$ $Q_h \propto Im(\varepsilon)\iiint |E|^2 dV$. Hence, the strong enhancement and deep penetration of the electric field could potentially lead to higher heat generation, even in the presence of

B. Yang, Q. Dai
CAS Key Laboratory of Nanophotonic Materials and Devices
CAS Key Laboratory of Standardization and Measurement for Nanotechnology
CAS Center for Excellence in Nanoscience
National Center for Nanoscience and Technology
Beijing 100190, China
E-mail: daiq@nanoctr.cn
B. Yang, Q. Dai
Center of Materials Science and Optoelectronics Engineering
University of Chinese Academy of Sciences
Beijing 100049, China
D. Pan
State Key Laboratory of Precision Spectroscopy
East China Normal University
Shanghai 200062, China
The ORCID identification number(s) for the author(s) of this article can be found under https://doi.org/10.1002/adom.202301080

DOI: 10.1002/adom.202301080

low material losses.[29] For instance, silicon nanospheres with Mie resonances have shown to be four times better at photothermal conversion than Au plasmonic counterparts.[30] Therefore, we anticipate that the strong field confinement of PhPs and deep field penetration into nanostructures could also cause significant heat generation. This aspect has been largely ignored so far, which could affect the performance of highly miniaturized nanophotonic devices relying on strong field confinement.

In this study, we explore the potential of polar dielectrics, specifically hexagonal boron nitride (hBN) antennas, as light-controllable heat sources in the mid-IR range. hBN, a polar crystal with low material loss and high thermal stability, is an excellent candidate for high-temperature IR nanophotonics.[31–33] The unique feature of hBN antennas lies in that they support a range of hyperbolic PhP (HPhPs) modes when exposed to mid-IR light. These HPhPs propagate with strong field confinement inside the antenna structure. Using finite element simulations, we demonstrate that an hBN nanorod can generate approximately 46 times more heat than a plasmonic Au counterpart of similar subwavelength dimensions ($\lambda/L \cong 5$). This significant improvement in heating performance is primarily attributed to the higher absorption efficiency and larger sizes of hBN nanorods. The dominant contribution comes from volume-confined HPhP modes, which outperform plasmonic heating by circumventing the electrostatic shielding effects, allowing for stronger field confinement and deeper field penetration. Additionally, we show that the heating performance of hBN antennas can be customized by adjusting various parameters such as incident light, hBN geometry, and material loss. By utilizing isotopically pure hBN with reduced material loss, a threefold increase in heat power can be achieved. These findings offer valuable insights into the mechanisms of photoinduced heating and open up new opportunities for designing efficient light-controllable heat sources utilizing materials that support PhPs.

2. Experimental Section

2.1. Calculation Method of the Heat Generation Power

When a photonic nanoparticle (NP) is illuminated, a portion of the incident light energy is scattered to the surrounding environment, while the remaining energy is absorbed by the NP and eventually dissipates as heat. The efficiency of these two processes is quantified by the scattering and absorption cross-sections, denoted as C_{sca} and C_{abs}, respectively. The heat generation power within the NP can be calculated as[28,34]

$$Q_{\mathrm{h}} = C_{\mathrm{abs}} I_0 = \frac{n_s^2 \omega}{2} \int_V \mathrm{Im}\left\{\epsilon(\mathbf{r},\omega)\right\} \left|\mathbf{E}(\mathbf{r})\right|^2 d\mathbf{r} \tag{1}$$

where $I_0 = n_s \epsilon_0 \, c|E_0|^2/2$ is the intensity of the incident light, E_0 is the amplitude of the incident plane wave, ϵ_0 is the vacuum permittivity, n_s is the refractive index of the surrounding medium, $\epsilon(\mathbf{r}, \omega)$ is the complex relative permittivity of the NP at the position r and light frequency ω, $E(\mathrm{r})$ is the electric field distributed inside the NP, and the integration is conducted for the heat power density ($\mathrm{q_h}$) over the NP's volume (V). In this work, the electric field distribution $E(\mathrm{r})$ is numerically computed using a finite element method.

The heat generation power (Q_{h}), as depicted in Equation (1), is determined by three crucial factors: the inherent material losses ($\mathrm{Im}(\epsilon)$), the electric field confinement ($|\boldsymbol{E}(\mathbf{r})|^2$), and the field distribution throughout the entire volume of the NP (V). It is worth noting that these factors are interconnected and should be carefully considered. For instance, a larger value of $\mathrm{Im}(\epsilon)$, indicating higher material loss, does not necessarily result in a higher heat power. This is because an increase in $\mathrm{Im}(\epsilon)$ simultaneously reduces the field intensity $|\boldsymbol{E}(\mathbf{r})|^2$ within the NP. Therefore, achieving a delicate balance among these three factors becomes imperative when striving to optimize photoinduced heat sources. By thoughtfully selecting materials and designing antennas to strike the right equilibrium, it is possible to maximize the photothermal efficiency of the heat source.

In the absence of phase transitions, the steady-state temperature distribution around the optically illuminated NPs is achieved through heat transfer with the surrounding environment. A general model describing the heating of a spherical NP from any photonic material by continuous wave illumination, coupled with a thermal diffusion equation, has been developed elsewhere.[10,35] In particular, the solution of the thermal diffusion equation in a steady-state regime provides a concise expression for the temperature rise at the NP[17,36]

$$\Delta T_{NP} = \frac{Q_{\mathrm{h}}}{4\pi\kappa_0 r_e} \tag{2}$$

where κ_0 is the thermal conductivity of the surrounding medium, which is much smaller than that of the NP; and r_{e} is the effective radius of the NP.

2.2. Permitivity of hBN

hBN is a promising polar dielectric for nanophotonic applications due to its unique properties, including low material loss, high thermal stability, and excellent electrical insulation.[32] As a representative of 2D van der Waals crystals, hBN has strong covalent bonds within each layer and weak van der Waals bonds between layers, resulting in a significant optical anisotropy. This anisotropy is characterized by opposite signs of permittivity along two perpendicular crystal axes, rendering hBN a natural hyperbolic material. In particular, hBN supports two types of zs within distinct frequency bands defined by the transverse-optical (TO) and longitudinal-optical (LO) phonon modes. These HPhPs arise due to the different signs in the permittivity components in hBN: Type I: $\epsilon_\perp > 0$, $\epsilon_\parallel < 0$; and Type II: $\epsilon_\perp < 0$, $\epsilon_\parallel > 0$) in the Reststrahlen bands (RBs). The in-plane and out-of-plane permittivity of hBN can be well described by the Lorentz model with the following expression[37]

$$\epsilon_{\mathrm{hBN},m} = \epsilon_{\infty,m}\left[1 + \frac{\left(\omega_{\mathrm{LO},m}\right)^2 - \left(\omega_{\mathrm{TO},m}\right)^2}{\left(\omega_{\mathrm{TO},m}\right)^2 - \omega^2 - i\omega\gamma_m}\right] \tag{3}$$

where the subscript $m = \perp$ or $\parallel$, denotes the in-plane and out-of-plane components corresponding to the perpendicular or parallel direction to the optical axis of the hBN crystal, respectively;

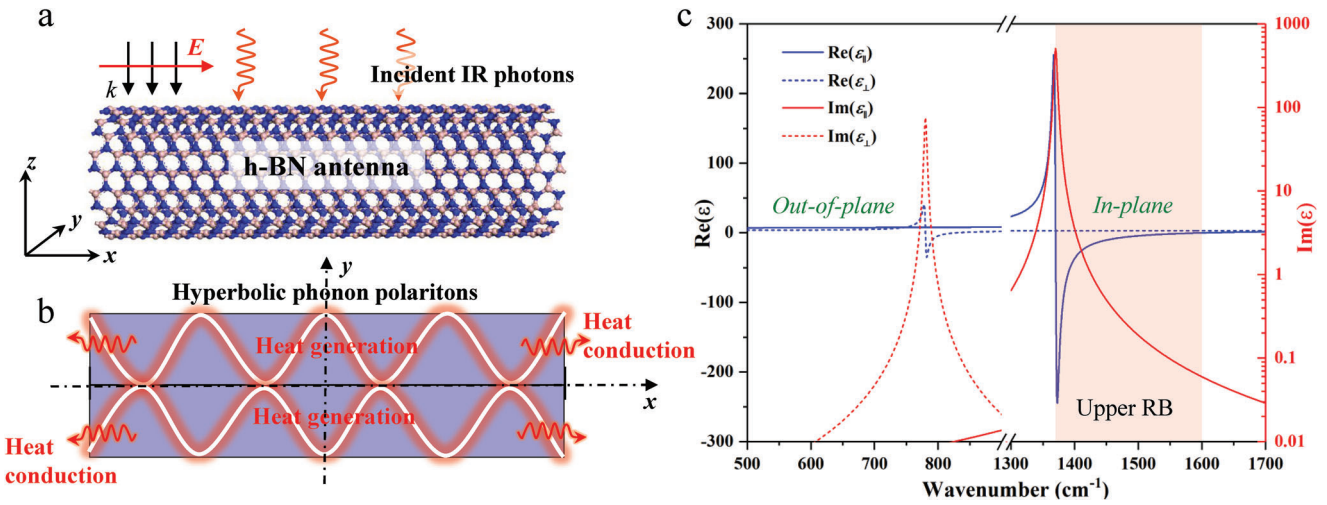

Figure 1. a) Illustration of a suspended hexagonal boron nitride (hBN) antenna exposed to the incident light with its electric field polarized parallel to the antenna's axis. b) Heat generation mediated by hyperbolic phonon polaritons (HPhPs) and the subsequent heat conduction in the hBN antenna. c) Frequency-dependent permittivity for naturally abundant hBN crystals, with the pink shaded area denoting the upper Reststrahlen band (RB) for in-plane permittivity.

$\epsilon_{\infty,m}$ is the high-frequency permittivity; $\omega_{LO,m}$ and $\omega_{TO,m}$ are the LO and TO phonon frequencies, respectively; and γ_m is the damping rate. The fitting parameters for hBN are given as $\epsilon_{\parallel,\infty} = 2.95$, $\omega_{LO,\parallel} = 830\ cm^{-1}$, $\omega_{TO,\parallel} = 780\ cm^{-1}$, and $\gamma_\parallel = 4\ cm^{-1}$ for the out-of-plane direction, while $\epsilon_{\perp,\infty} = 4.87$, $\omega_{LO,\perp} = 1610\ cm^{-1}$, $\omega_{TO,\perp} = 1370\ cm^{-1}$, and $\gamma_\perp = 5\ cm^{-1}$ for the in-plane direction.[38,39]

The thermophysical properties of hBN have been extensively reported in previous literature.[40] One notable aspect is the highly anisotropic thermal conductivity of hBN, with a relatively high value along the in-plane direction (approximately 300–400 W (m K)$^{-1}$) and a significantly lower value along the out-of-plane direction (approximately 2–30 W (m K) $^{-1}$). For the hBN antenna depicted in **Figure 1**a, this work assumes axial and radial thermal conductivity values of 400 and 20 W (m K) $^{-1}$, respectively.[41] Note that both the permittivity and the thermophysical properties of hBN are considered to be temperature independent in the subsequent calculations.

2.3. Model Validation

Here, a 3D numerical model that couples the electromagnetism and heat transfer module had been built by using the commercial software COMSOL Multiphysics. The finite element method (FEM) was employed to solve the governing equations. To ensure the accuracy and reliability of the model, it was first validated against analytical solutions for a 20 nm-diameter gold nanosphere in water. The simulation results, including optical responses (e.g., absorption cross-section) and the resulting temperature rise, showed good agreement with the analytical solutions (Figure S1, Supporting Information). This rigorous validation process establishes a solid foundation for employing the numerical model in the investigation of hBN antennas and their performance analysis.

3. Results and Discussions

3.1. Phonon Polariton Modes and Subsequent Heating Effects in hBN Nanorods

We begin by studying the optical and thermal behaviors of an hBN nanorod (hBNNR) when subjected to far-field CW IR light. The electric field of the incident light is polarized along the nanorod axis (Figure 1a). Our main focus is to analyze its response to light frequencies ranging from 1300 and 1600 cm^{-1}, which corresponds to the upper RB of hBN. Unless specified otherwise, the intensity of the incident light is set to $5 \times 10^7\ W\ m^{-2}$. Further simulation details can be found in the Supporting Information.

Figure 2 shows the optical and thermal responses of a suspended hBNNR with a length of 720 nm and a diameter of 100 nm in air. The heat power spectrum exhibits multiple sharp peaks that decrease as the light frequency increases (Figure 2a). The insets (Figure 2a i-iii) visually depict the normalized electric field intensity, i.e., the field enhancement ($|E/E_0|^2$), on a mid-Z cross-section for each peak. They display characteristic sinusoidal patterns inside the nanorod and exponential decay outside, indicating the presence of volume-confined HPhPs within the hBNNR. Along the nanorod axis, the field amplitude experiences strong oscillations, with an increased number of maxima and minima at higher frequencies, and a reduced distance between them (Figure S2, Supporting Information). This behavior signifies a frequency-dependent standing-wave pattern known as longitudinal Fabry–Pérot (FP) cavity modes within the hBNNR.[25] These FP modes have different orders based on how many times HPhPs travel along the axis and reflect from the ends.[42] Similar interference patterns have been experimentally observed in other structures, including hBN nanorods,[25] hBN nanotubes,[42] and carbon nanotubes,[43] using IR scattering-type scanning near-field optical microscopy. However, it is important to note that

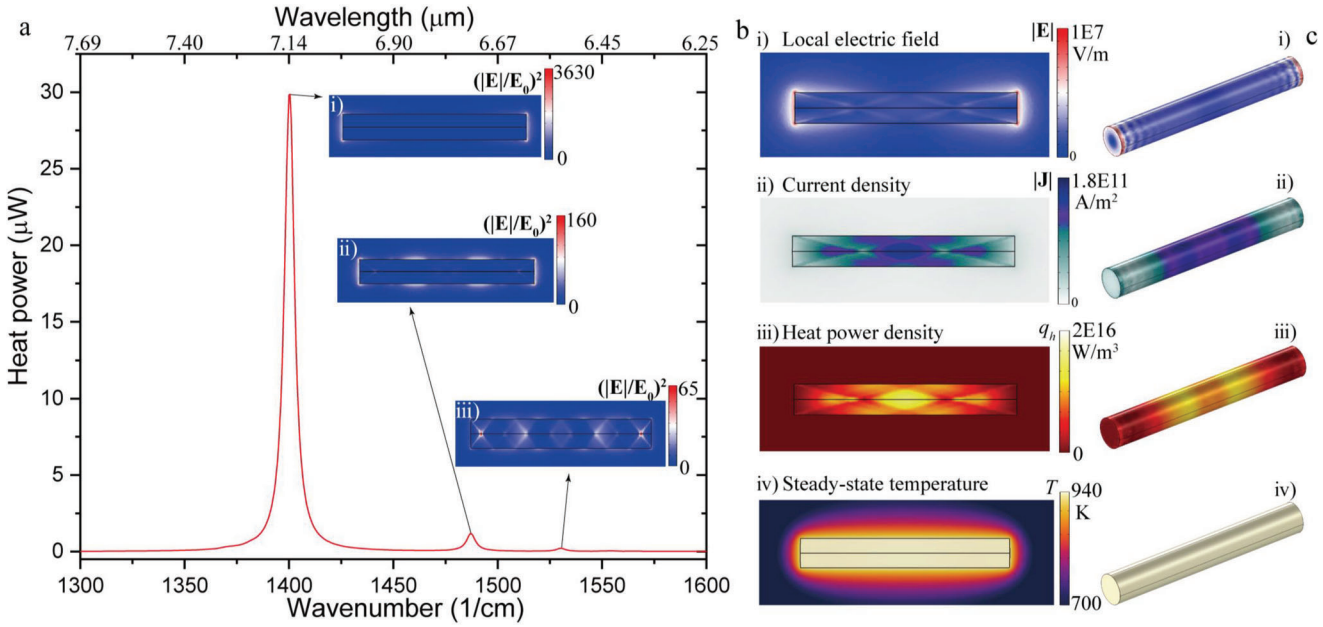

Figure 2. Optical and thermal responses of an hexagonal boron nitride nanorod (hBNNR) with $L = 720$ nm and $d = 100$ nm, surrounded by air. a) The absorption/heat generation power spectrum of the hBNNR, with insets showing the distribution of near-field electric field ($|E|$) at peak frequencies of i) 1400 cm^{-1}, ii) 1487 cm^{-1}, and iii) 1530 cm^{-1}, corresponding to the dipolar, quadrupolar, and hexapolar modes, respectively. b) Distributions of i) local electric field, ii) current density, iii) heat power density, and iv) steady-state temperature for the 2D-cut cross-section at mid-Z plane at the dipolar resonant frequency of 1400 cm^{-1}. c) Corresponding field distributions on the nanorod surface.

the patterns resulting from tip-launched polaritons differ from those depicted in Figure 2a, as they are influenced by the position of the tip. The first-order dipolar FP mode of HPhPs, occurring at around 1400 cm^{-1}, exhibits the highest absorption, resulting in a peak heat power of approximately 29.8 μW. This enhanced absorption is attributed to the strong confinement of the local field by HPhPs within the hBNNR. The insets reveal that the field enhancement reaches values of about 3638, 161, and 64 for these three FP modes, resulting in a reduction in heat power from approximately 29.8 to 1.2 μW, and even to as low as 0.2 μW, respectively. This result highlights the strong dependence of HPhP-mediated heating on the frequency of the incident light, enabling flexible control of heating by simply adjusting the light frequency. Furthermore, the narrow linewidth of these HPhP-mediated peaks makes the hBNNR a promising candidate for light-driven thermal switches by manipulating the light frequency.

To gain a deeper understanding of the physical mechanisms underlying the photoinduced heating in the hBNNR, the distributions of the local electric field, current density, and heat power density for the dipolar FP mode are examined in Figure 2b,c. Notably, the similarity in the distributions between the current density and heat power density (Figure 2b ii-iii) indicates that the heat generation arises from the electric current driven by the electric field confined within the hBNNR. In contrast, the surface-confined electric field, despite being much stronger, has a negligible impact on the distribution of heat power intensity. This behavior is reminiscent of plasmonic heating observed in metal nanostructures, where the field enhancement and resultant heating mediated by LSPs are mainly restricted to shallow surface areas.[14,17,35,44] This distinction highlights the fact that the HPhP modes in hBNNR differ significantly from LSPs in metals, as they possess a volume-confined electric field extending beyond the surface. Consequently, HPhPs have the potential to generate heat much more efficiently than LSPs. The subsequent section will explore this distinction further when investigating how geometry influences this heating effect.

After the excitation of HPhP modes, the concentrated photonic energy within the hBNNR undergoes rapid decay and is converted into heat through scattering between optical and acoustic phonons. Subsequently, the generated heat in the hBNNR dissipates quickly, causing the temperature of the hBNNR to change over time until it reaches a thermal equilibrium with its surroundings. For the specific hBNNR presented in Figure 2, the steady-state temperature can reach up to about 940 K (Figure 2b iv,c iv). These findings suggest that the hBNNR serves as an efficient heat source that can be remotely controlled using IR light and exhibits a high degree of tunability. Similar optical and thermal responses mediated by HPhPs for the hBNNR suspended in water can be found in Figure S3 (Supporting Information).

3.2. Geometry-Dependent Responses and Comparison with Plasmonic Heating

In this section, we explore the impact of hBN antenna geometry on the HPhP-mediated heating under IR light excitation. We consider two scenarios: (1) adjusting the length of hBNNRs while maintaining a fixed diameter of 100 nm, and (2) varying the wall thickness of hollow hBN nanotubes with a fixed length of 720 nm and outer diameter of 100 nm.

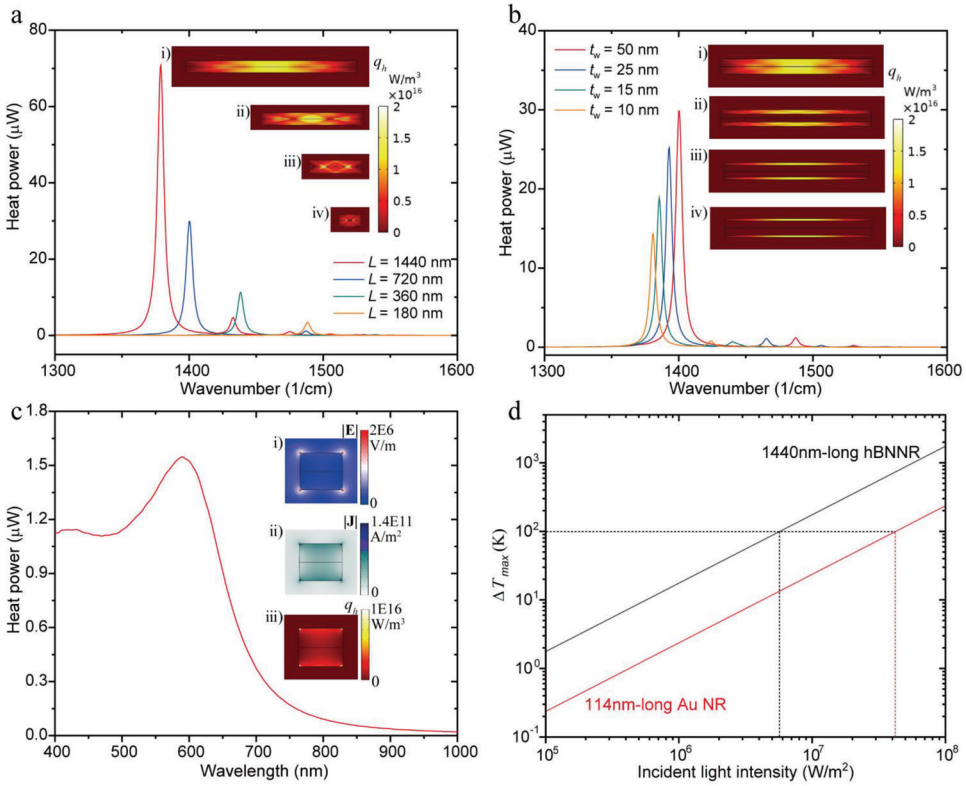

Figure 3. a,b) Geometry-dependent heating mediated by hyperbolic phonon polaritons (HPhPs): heat generation power of hexagonal boron nitride (hBN) antennas with varying a) lengths of hBN nanorods (hBNNRs) and b) wall thicknesses of hBN nanotubes, with insets showing the corresponding distributions of heat power density q_h for their dipolar resonant modes (mid-Z plane). c) Plasmonic heating for a 114 nm long Au NR, with insets showing related field distributions at its resonant wavelength of 590 nm ($\lambda/L = 5$). d) Comparison of maximized temperature rise ΔT_{max} for the 1440 nm long hBNNR and 114 nm long Au NR as a function of incident light intensity.

By modifying the length of hBNNRs, we can tailor their optical and thermal responses. **Figure 3**a illustrates that increasing the length of hBNNRs leads to a redshift in the resonant peaks of the dipolar FP modes and an increase in heat generation power. This behavior arises from the hBNNRs functioning as longitudinal-FP cavity resonators for HPhPs, which bounce back and forth between the two terminals of the nanorods. The longitudinal FP modes can be described by equation[45] $2k_pL + 2\varnothing_R = 2\pi l$, where $k_p = 2\pi/\lambda_p$ is the wavevector, $\varnothing_R$ is the reflection phase shift, and l is the resonance order. With an increase in length, the resonance frequency decreases, causing a redshift of the resonant peaks for a given mode number. Moreover, longer nanorods facilitate the propagation of HPhPs along extended paths, resulting in increased heat generation as the energy carried by HPhPs dissipates. The longest nanorod, with a length of 1440 nm, exhibits a heat power of approximately 70.84 μW, which is 20 times higher than the 180 nm long nanorod with a heat power of ≈3.43 μW (Figure 3a).

The wall thickness of hollow hBN nanotubes (hBNNTs) also plays a crucial role in their photothermal conversion performance. Figure 3b demonstrates that reducing the wall thickness of hBNNTs from 50 nm (nanorod) to 10 nm (nanotube) leads to a redshift of the resonant peaks of the dipolar HPhP modes. This redshift can be attributed to the effective permittivity change caused by introducing a hollow air channel within the hBN antenna that modifies its dielectric environment.[46] Additionally, the reduction in wall thickness also results in a decrease in the heat power at the dipolar HPhP mode peaks, due to the reduced amount of hBN volume available for heating in nanotubes with thinner walls. The insets of q_h field distributions in Figure 3a,b provide visual evidence that the maximum heat power density originates from the electric field locally confined inside the hBNNRs, rather than outside. This confirms the dominant contribution of volume-confined HPhP modes to heat generation. Furthermore, it is worth noting that hBNNRs exhibit a higher concentration of confined HPhP modes compared to hollow BNNTs, with a deeper field penetration into the nanostructures (Figure S5, Supporting Information). This unique characteristic makes hBNNR a more efficient light-controllable heat source compared to hBNNTs.

In addition, we compare the heating performance of hBN antennas mediated by volume-confined HPhPs with that of metal nanostructures mediated by LSPs (Figure 3c,d). Specifically, we compare a 114 nm long Au nanorod (AuNR) and a 1440 nm long hBNNR, both having a length relative to their wavelength (λ/L) of about 5 under resonant illuminations. The absorption efficiency of the AuNR (≈2.7) is approximately 1/4 of that of the hBNNR (≈9.8) (Figure S3, Supporting Information). The insets show that the heat generated in the AuNR is primarily concentrated in a shallow surface area where the electric field is strong.

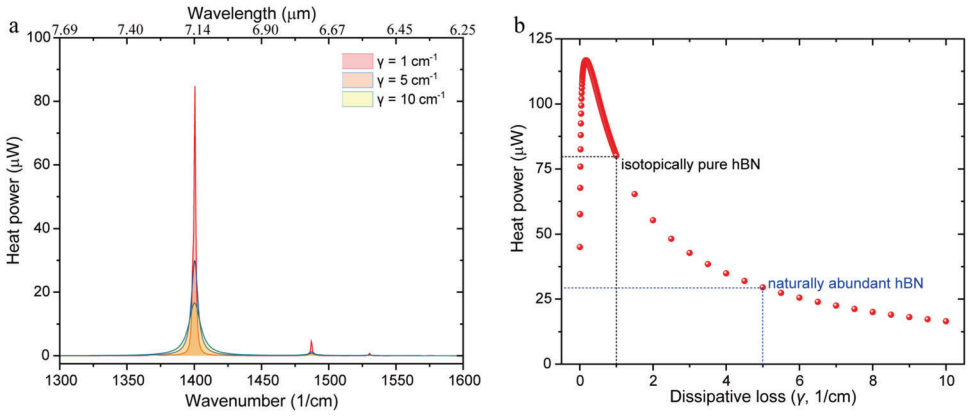

Figure 4. Effects of inherent material losses on the hyperbolic phonon polaritons (HPhP) modes mediated heating in the 720 nm long hexagonal boron nitride nanorod (hBNNR). a) Heat power spectra under damping rate of 1, 5, and 10 cm^{-1}. b) Heat power generated as a function of damping rate (γ) of the in-plane permittivity for hBN.

This characteristic makes it more challenging to heat thicker and larger nanostructures due to static electric shielding.[17] In metal nanostructures, the electric field enhancement is limited to the skin depth, resulting from their high free carrier concentrations. In contrast, the hBN antennas exhibit heating throughout their volume (Figure 3a,b), because they support HPhPs that tightly confine the electric field inside them (Figure S5, Supporting Information). As a result, the hBNNR produces a heat power of 70.84 μW, which is approximately 46 times higher than that of the AuNR (1.55 μW), as shown in Figure 3a,c. This significant difference is attributed to both the higher absorption efficiency and the larger size of the hBNN. Consequently, the hBNNR reaches a much higher steady-state temperature than the AuNR (Figure 3d), implying that it can achieve the same temperature using less light and thus save more energy. The key point is that to make hBN antennas more efficient heat sources, it is crucial to optimize the electric field inside them (Equation 1) mediated by volume-confined HPhPs, rather than outside.

We would like to stress that other dielectric materials exhibiting robust PhPs and low material losses, such as SiC, SiO_2, α-MoO_3, and many others, are also promising candidates for efficient light-controllable heat sources. To further support this notion, we conducted additional comparisons of the optical heating performance among hBN, Au, and SiO_2 nanorods. These nanorods have an identical length of 720 nm and similar resonant frequencies in the mid-IR range. The corresponding results are illustrated in Figure S6 (Supporting Information). These comparisons further confirm the superiority of PhPs over plasmons for light-controllable heat sources and demonstrate that the presence of hyperbolic dispersion in specific materials enables further improvement in heat generation by facilitating the volumetric confinement of polaritons. These results highlight the potential of exploiting PhPs and their hyperbolic dispersion for efficient IR photothermal applications.

3.3. Optimized PhP-Mediated Heating by Loss Engineering

In this section, we explore the impact of dissipative losses in photonic materials on the HPhPs-mediated heating performance. Previous efforts to mitigate these losses have involved employing isotopically pure materials[24,47] and operating under cryogenic conditions[26] to improve the performances of PhPs, such as extending their lifetimes and propagation distances. However, our findings reveal an intriguing observation: these loss reduction techniques can also lead to increased photoinduced heat generation. For instance, **Figure 4**a shows that at $\gamma = 1$ cm^{-1}, typical for isotopically pure hBN, the peak heat power is approximately 85 μW.[24] This represents a threefold increase in heat power compared to the initial scenario (Figure 2a) with a higher loss rate ($\gamma = 5$ cm^{-1}) for naturally abundant hBN. This finding suggests that reducing material losses may not always be advantageous for nanophotonic devices, particularly when considering the accompanying heat generation.

We also conduct calculations to determine the heat power of an hBNNR with varying dissipative losses when exposed to light at its dipolar resonant frequency. In Figure 4b, we observe that as the damping rate γ decreases from 10 to 0.001 cm^{-1}, the heat power initially increases, but then sharply drops off as it approaches zero. The optimal heat power, approximately 117 μW, is attained at a relatively small loss of $\gamma = 0.17$ cm^{-1}. This trend highlights the trade-off between material loss and field confinement inside the photonic antenna (Equation 1). The optimal balance between these two factors is achieved by avoiding two limit cases: $\mathrm{Im}(\epsilon)\to 0$ or $\mathrm{Im}(\epsilon)\to\infty$ ($|E(\mathrm{r})| \to 0$). In the former scenario, HPhP modes propagate indefinitely with no loss, resulting in no energy dissipation and, therefore, no heat generation. Conversely, in the latter scenario, minimal electric field confinement exists inside the antenna, leading to a lack of energy concentration that can be dissipated as heat. These findings provide valuable insights for the design of novel optimized nanostructures using dielectrics for both nanophotonic and photothermal applications.

4. Conclusions

In summary, our study highlights the potential of dielectric antennas as efficient light-controlled heat sources when illuminated by monochromatic light at their resonant frequencies. This unique functionality arises from the excitation and damping of

PhPs, which effectively concentrate and dissipate incident photonic energy within the antenna, resulting in heat generation through intrinsic loss mechanisms. Notably, our investigations reveal that hBNNRs outperform gold counterparts, exhibiting a significant 46-fold increase in heat power, owing to their enhanced absorption capacity and larger size. This PhP-mediated heating offers distinct advantages over plasmonic heating, including volumetric heating capability and high efficiency, by circumventing limitations imposed by the electrostatic shielding effect in plamonic materials. Moreover, the heating performance of hBN antennas can be further optimized by tailoring their size, geometry, and material loss characteristics. Overall, our findings provide valuable insights into PhP-mediated heating and open exciting avenues for designing light-controlled heat sources utilizing materials that support PhPs, holding great promise for efficient IR photothermal applications.

Supporting Information

Supporting Information is available from the Wiley Online Library or from the author.

Acknowledgements

The authors gratefully acknowledge the financial support from the National Key Research and Development Program of China (Grant No. 2022YFE0129700), the National Natural Science Foundation of China (Grant No. 51925203), the Strategic Priority Research Program of the Chinese Academy of Sciences (Grant No. XDB36000000), and the Special Research Assistant Program of the Chinese Academy of Sciences.

Conflict of Interest

The authors declare no conflict of interest.

Data Availability Statement

The data that support the findings of this study are available from the corresponding author upon reasonable request.

Keywords

hBN antennas, heat sources, phonon polaritons, photothermal conversion, thermonanophotonics

Received: May 8, 2023
Revised: July 6, 2023
Published online: July 28, 2023

[1] Y. Bai, J. Yin, J.-X. Cheng, *Sci. Adv.* **2021**, *7*, eabg1559.
[2] H. Zong, C. Yurdakul, Y. Bai, M. Zhang, M. S. Ünlü, J. Cheng, *ACS Photonics* **2021**, *8*, 3323.
[3] S. Yoshiaki, *J. Mater. Chem. C* **2022**, *10*, 451.
[4] J. A. Campos-Gonzalez-Angulo, R. F. Ribeiro, J. Yuen-Zhou, *Nat. Commun.* **2019**, *10*, 4685.
[5] B. Xiang, R. F. Ribeiro, M. Du, L. Chen, Z. Yang, J. Wang, J. Yuen-Zhou, W. Xiong, *Science* **2020**, *368*, 665.
[6] F. Neubrech, C. Huck, K. Weber, A. Pucci, H. Giessen, *Chem. Rev.* **2017**, *117*, 5110.
[7] A. Bylinkin, M. Schnell, M. Autore, F. Calavalle, P. Li, J. Taboada-Gutièrrez, S. Liu, J. H. Edgar, F. Casanova, L. E. Hueso, P. Alonso-Gonzalez, A. Y. Nikitin, R. Hillenbrand, *Nat. Photonics* **2021**, *15*, 197.
[8] T. Chen, M. Du, Z. Yang, J. Yuen-Zhou, W. Xiong, *Science* **2022**, *378*, 790.
[9] G. Baffou, R. Quidant, *Laser Photonics Rev.* **2013**, *7*, 171.
[10] G. Baffou, *Thermoplasmonics: Heating Metal Nanoparticles Using Light*, Cambridge University Press, Cambridge **2018**.
[11] B. Yang, C. Li, Z. Wang, Q. Dai, *Adv. Mater.* **2022**, *34*, 2107351.
[12] G. Baffou, F. Cichos, R. Quidant, *Nat. Mater.* **2020**, *19*, 946.
[13] L. Jauffred, A. Samadi, H. Klingberg, P. M. Bendix, L. B. Oddershede, *Chem. Rev.* **2019**, *119*, 8087.
[14] G. Baffou, C. Girard, R. Quidant, *Phys. Rev. Lett.* **2010**, *104*, 136805.
[15] S. D. Lounis, E. L. Runnerstrom, A. Llordés, D. J. Milliron, *J. Phys. Chem. Lett.* **2014**, *5*, 1564.
[16] S. A. Maier, *Nanoplasmonics: Fundamentals and Applications*, Springer, Berlin **2007**.
[17] G. Baffou, R. Quidant, C. Girard, *Appl. Phys. Lett.* **2009**, *94*, 153109.
[18] J. S. Donner, G. Baffou, D. McCloskey, R. Quidant, *ACS Nano* **2011**, *5*, 5457.
[19] G. V. Naik, V. M. Shalaev, A. Boltasseva, *Adv. Mater.* **2013**, *25*, 3264.
[20] D. Jing, D. Song, *Renewable Sustainable Energy Rev.* **2017**, *78*, 452.
[21] E. Cortés, F. J. Wendisch, L. Sortino, A. Mancini, S. Ezendam, S. Saris, L. de S. Menezes, A. Tittl, H. Ren, S. A. Maier, *Chem. Rev.* **2022**, *122*, 15082.
[22] T. Low, A. Chaves, J. D. Caldwell, A. Kumar, N. X. Fang, P. Avouris, T. F. Heinz, F. Guinea, L. Martin-Moreno, F. Koppens, *Nat. Mater.* **2017**, *16*, 182.
[23] W. Ma, P. Alonso-González, S. Li, A. Y. Nikitin, J. Yuan, J. Martín-Sánchez, J. Taboada-Gutiérrez, I. Amenabar, P. Li, S. Vélez, C. Tollan, Z. Dai, Y. Zhang, S. Sriram, K. Kalantar-Zadeh, S. T. Lee, R. Hillenbrand, Q. Bao, *Nature* **2018**, *562*, 557.
[24] A. J. Giles, S. Dai, I. Vurgaftman, T. Hoffman, S. Liu, L. Lindsay, C. T. Ellis, N. Assefa, I. Chatzakis, T. L. Reinecke, J. G. Tischler, M. M. Fogler, J. H. Edgar, D. N. Basov, J. D. Caldwell, *Nat. Mater.* **2018**, *17*, 134.
[25] F. J. Alfaro-Mozaz, P. Alonso-González, S. Vélez, I. Dolado, M. Autore, S. Mastel, F. Casanova, L. E. Hueso, P. Li, A. Y. Nikitin, R. Hillenbrand, *Nat. Commun.* **2017**, *8*, 15624.
[26] G. Ni, A. S. McLeod, Z. Sun, J. R. Matson, C. F. B. Lo, D. A. Rhodes, F. L. Ruta, S. L. Moore, R. A. Vitalone, R. Cusco, L. Artús, L. Xiong, C. R. Dean, J. C. Hone, A. J. Millis, M. M. Fogler, J. H. Edgar, J. D. Caldwell, D. N. Basov, *Nano Lett.* **2021**, *21*, 5767.
[27] J. B. Khurgin, *Nat. Nanotechnol.* **2015**, *10*, 2.
[28] G. P. Zograf, M. I. Petrov, S. V. Makarov, Y. S. Kivshar, *Adv. Opt. Photonics* **2021**, *13*, 643.
[29] A. Lalisse, G. Tessier, J. Plain, G. Baffou, *J. Phys. Chem. C* **2015**, *119*, 25518.
[30] G. P. Zograf, M. I. Petrov, D. A. Zuev, P. A. Dmitriev, V. A. Milichko, S. V. Makarov, P. A. Belov, *Nano Lett.* **2017**, *17*, 2945.
[31] R. Starko-Bowes, X. Wang, Z. Xu, S. Pramanik, N. Lu, T. Li, Z. Jacob, *Nano Lett.* **2019**, *19*, 8565.
[32] J. D. Caldwell, I. Aharonovich, G. Cassabois, J. H. Edgar, B. Gil, D. N. Basov, *Nat. Rev. Mater.* **2019**, *4*, 552.
[33] B. Yang, Q. Dai, *Nanoscale* **2022**, *14*, 16978.
[34] X. Chen, Y. Chen, M. Yan, M. Qiu, *ACS Nano* **2012**, *6*, 2550.
[35] G. Baffou, R. Quidant, F. J. García De Abajo, *ACS Nano* **2010**, *4*, 709.
[36] A. O. Govorov, H. H. Richardson, *Nano Today* **2007**, *2*, 30.
[37] B. Yang, D. Pan, X. Guo, H. Hu, Q. Dai, *Int. J. Therm. Sci.* **2022**, *176*, 107493.

[38] P. Li, I. Dolado, F. J. Alfaro-Mozaz, F. Casanova, L. E. Hueso, S. Liu, J. H. Edgar, A. Y. Nikitin, S. Vélez, R. Hillenbrand, *Science* **2018**, *359*, 892.
[39] Z. Yuan, R. Chen, P. Li, A. Y. Nikitin, R. Hillenbrand, X. Zhang, *ACS Photonics* **2020**, *7*, 2610.
[40] S. K. Singh, M. Neek-Amal, S. Costamagna, F. M. Peeters, *Phys. Rev. B: Condens. Matter Mater. Phys.* **2013**, *87*, 184106.
[41] X. G. Xu, B. G. Ghamsari, J. H. Jiang, L. Gilburd, G. O. Andreev, C. Zhi, Y. Bando, D. Golberg, P. Berini, G. C. Walker, *Nat. Commun.* **2014**, *5*, 4782.
[42] C. Phillips, Y. F. Lai, G. C. Walker, *J. Phys. Chem. Lett.* **2021**, *12*, 11683.
[43] I.-H. Lee, M. He, X. Zhang, Y. Luo, S. Liu, J. H. Edgar, K. Wang, P. Avouris, T. Low, J. D. Caldwell, S.-H. Oh, *Nat. Commun.* **2020**, *11*, 3649.
[44] J. Cunha, T. L. Guo, A. N. Koya, A. Toma, M. Prato, G. D. Valle, A. Alabastri, R. P. Zaccaria, *Adv. Opt. Mater.* **2020**, *8*, 2001225.
[45] S. Wang, F. Wu, K. Watanabe, T. Taniguchi, C. Zhou, F. Wang, *Nano Lett.* **2020**, *20*, 2695.
[46] C. Phillips, L. Gilburd, X. G. Xu, G. C. Walker, *J. Phys. Chem. Lett.* **2019**, *10*, 4851.
[47] C. W. Chang, A. M. Fennimore, A. Afanasiev, D. Okawa, T. Ikuno, H. Garcia, D. Li, A. Majumdar, A. Zettl, *Phys. Rev. Lett.* **2006**, *97*, 085901.